Nanoelectronics and Its New Materials – A NEW ERA OF NANOSCIENCE

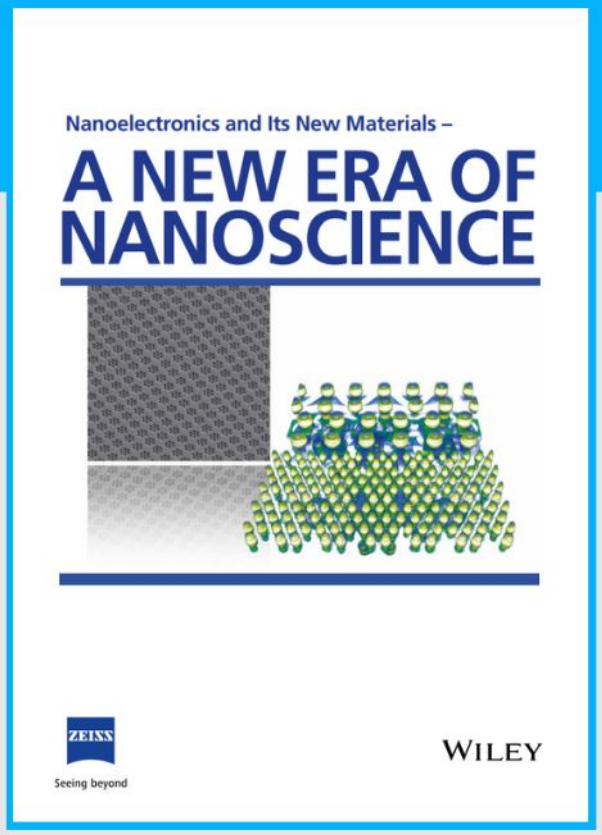

Discover the recent advances in electronics research and fundamental nanoscience.

Nanotechnology has become the driving force behind breakthroughs in engineering, materials science, physics, chemistry, and biological sciences. In this compendium, we delve into a wide range of novel applications that highlight recent advances in electronics research and fundamental nanoscience. From surface analysis and defect detection to tailored optical functionality and transparent nanowire electrodes, this eBook covers key topics that will revolutionize the future of electronics.

To get your hands on this valuable resource and unleash the power of nanotechnology, simply download the eBook now. Stay ahead of the curve and embrace the future of electronics with nanoscience as your guide.

ZEISS

Seeing beyond

WILEY

ADVANCED FUNCTIONAL MATERIALS
www.afm-journal.de

Interfacial Pyro-Phototronic Effect: A Universal Approach for Enhancement of Self-Powered Photodetection Based on Perovskites with Centrosymmetry

Linjuan Guo, Huan Wang, Ziqing Xu, Ridong Cong, Lei Zhao, Suheng Zhang, Kai Zhang, Linjie Gao, Shufang Wang, Caofeng Pan,* and Zheng Yang**

Utilizing the pyro-phototronic effect presents a potent approach to augment the efficacy of self-powered photodetectors (PDs) that rely on metal halide perovskites (MHPs). Nevertheless, the pyro-phototronic effect has thus far been restricted to perovskites possessing a non-centrosymmetric crystal structure, limiting their scope of application. This study introduces a universal interfacial pyro-phototronic effect (IPPE) strategy to MHP single crystals with centrosymmetry. The utilization of heterojunctions or Schottky junctions has resulted in the observation of typical four-stage photoresponses with rapid speed, thereby significantly enhancing the performance of self-powered PDs and expanding the spectral response range. The contact conditions, such as the choice of metals and surface smoothness, have an important impact on IPPE. The IPPE approach is a versatile technique that can be employed to fabricate self-powered PDs based on diverse 3D and 2D perovskites. This study broadens the utilization of the pyro-phototronic phenomenon in centrosymmetric perovskites, which offer advantages in producing optoelectronic devices with superior performance.

1. Introduction

Self-powered photodetectors (PDs) possess a straightforward device structure, reduced device weight, and significantly lower energy consumption, enabling them to operate without external energy sources. Furthermore, their ability to harness light energy from the surrounding environment renders them highly suitable for wireless photodetection, chemical sensing, in situ medical therapy monitoring, and integration into advanced sensor networks.[1–3] To realize high-performance and self-powered photodetection, it is common practice to fabricate heterojunctions or Schottky junctions that possess robust built-in electric fields. Additionally, the modulation of the energy band structure at the interface through physical phenomena, such as the piezo-phototronic effect[4–7] and pyro-phototronic effect,[8–11] can significantly enhance photodetection capabilities. And the pyro-phototronic effect is particularly potent, as the light-induced pyroelectric charges can effectively manipulate the built-in electric field. Thus, modifying the optoelectronic processes of the photo-generated charge carriers.[12] The pyroelectric effect has been utilized in various applications such as thermal imaging, infrared sensing, and energy harvesting due to its ultra-fast response time down to picoseconds.[13] Consequently, it is possible to achieve self-powered photodetection with improved responsivity, reduced response time, and expanded response spectrum. Moreover, the pyro-phototronic effect can be combined with ferroelectricity,[14] piezoelectricity,[4] or flexoelectricity[15] to further enhance the PDs' performance.

Metal halide perovskites (MHPs) have recently garnered considerable attention for their diverse optoelectronic applications, including solar cells, lasers, light-emitting diodes, and PDs. This is attributed to their great light absorption coefficient, high carrier mobility, long carrier diffusion length, low trap density, and adjustable bandgap.[16–21] Additionally, similar to their oxide counterparts, several MHPs exhibit piezoelectric or ferroelectric polarizations.[22,23] Furthermore, halide perovskite-based PDs currently utilize the pyro-phototronic effect. Our research group has successfully demonstrated the efficacy of several high-performance perovskite-based PDs utilizing the pyro-phototronic effect, as evidenced by previous studies.[24–28] Luo's research group has presented a series of 2D cesium-based perovskite ferroelectrics that exhibit unique ferro-pyro-phototronic properties.[29]

L. Guo, H. Wang, Z. Xu, R. Cong, L. Zhao, S. Zhang, K. Zhang, L. Gao, S. Wang, Z. Yang
Hebei Key Laboratory of Optic-Electronic Information and Materials
National & Local Joint Engineering Laboratory of New Energy Photoelectric Devices
College of Physics Science and Technology
Hebei University
Baoding 071002, P. R. China
E-mail: sfwang@hbu.edu.cn; yangzheng06@hbu.edu.cn

C. Pan, Z. Yang
CAS Center for Excellence in Nanoscience
Beijing Institute of Nanoenergy and Nanosystems
Chinese Academy of Sciences
Beijing 100083, P. R. China
E-mail: cfpan@binn.cas.cn

The ORCID identification number(s) for the author(s) of this article can be found under https://doi.org/10.1002/adfm.202306526

DOI: 10.1002/adfm.202306526

However, the application range of the pyro-phototronic effect is often limited by crystal symmetry, particularly in non-centrosymmetric perovskites, which significantly restricts its potential. As a result, effective methods to enhance the performance of self-powered PDs in perovskites with a cubic structure, such as $MAPbBr_3$ and $MAPbCl_3$, are currently scarce. Marin Alexe's group recently presented evidence that the band bending at Schottky junction interfaces can induce polar symmetry, leading to piezoelectricity and pyroelectricity in centrosymmetric materials.[30] The coefficients of the induced piezoelectric and pyroelectric effects are highly dependent on the electrostriction coefficient of the materials. Notably, MHP single crystals (SCs) exhibited a high electrostriction coefficient.[31] Theoretically, interfacial piezoelectric effect can also be generated in halide perovskites with a cubic structure, which requires further investigation. Besides, as a similar polarization property, the interfacial piezoelectric effect in MHPs is also expected. Also, the influence of Schottky junction conditions on interfacial pyroelectric effect, has not been deeply studied. Furthermore, it is anticipated that the interfacial pyro-phototronic effect (IPPE) will be present in perovskite-based heterojunctions with band bending at the interface, in conjunction with the construction of Schottky junctions, necessitating comprehensive investigation.

This study showcases a universal IPPE approach for self-powered photodetection utilizing various centrosymmetric MHP semiconductors, including 3D perovskites such as $MAPbBr_3$ and $MAPbCl_3$, as well as 2D perovskites like $(PEA)_2PbI_4$. The observation of pyro-phototronic effect-enhanced photoresponses can be achieved by fabricating heterojunctions or Schottky junctions utilizing MHP SCs with centrosymmetry. Additionally, the spectral response wavelength range can be extended beyond the absorption limit of the material. The pertinent operational mechanisms were subjected to meticulous analysis. It is found that the contact conditions, such as the choice of metals and surface smoothness, have an important impact on IPPE. This study broadens the utilization of the pyro-phototronic effect in diverse MHPs-based PDs, without limitations imposed by crystal symmetry, thereby offering an efficacious avenue for photodetection and optical communication applications with superior performance.

2. Results and Discussion

This study utilized three representative MHPs possessing symmetrical crystal structures, specifically $MAPbBr_3$, $MAPbCl_3$, and $(PEA)_2PbI_4$, as models for the development of IPPE-based self-powered PDs. The $MAPbBr_3$ and $MAPbCl_3$ single crystals were grown with and without substrates using an inversed temperature crystallization method, while the $(PEA)_2PbI_4$ single crystals were prepared via a solution temperature-lowering method. The experimental procedures for the growth of these SCs are described in detail in the Experimental Section. Figure S1a,d, Supporting Information depict the $MAPbBr_3$ SC and $MAPbCl_3$ SC, respectively, exhibiting a uniform shape without any discernible flaws. From the absorption spectra in Figure S1b,e, Supporting Information, the corresponding bandgap of 2.21 eV for $MAPbBr_3$ SC and 2.94 eV for $MAPbCl_3$ SC can be deduced. At the same time, the peaks of the photoluminescence (PL) spectra are located at ≈571 and 410 nm, respectively. Then, the cubic crystal structures of the $MAPbBr_3$ SC and $MAPbCl_3$ SC were confirmed via the X-ray diffraction (XRD) spectra. As shown in Figure S1c, Supporting Information, the XRD pattern of $MAPbBr_3$ SC measured on the maximal facet of the SC shows only (100), (200), and (300) diffraction peaks, with the corresponding 2θ located at 15.02°, 30.22°, and 46.01°, respectively. For $MAPbCl_3$ SC, the results are similar, with the corresponding 2θ located at 16.04°, 31.78°, and 48.4°, respectively (Figure S1f, Supporting Information). The XRD patterns demonstrate the single-crystalline nature of the aforementioned crystals, which exhibit exposed crystal faces of (100). The aforementioned characterizations collectively indicate the successful growth of high-quality $MAPbBr_3$ and $MAPbCl_3$ SCs possessing a symmetrical crystal structure. However, residual liquids may adhere to the crystals during extraction from the stock solution, resulting in additional crystallization and rough surfaces. To ensure optimal contact between the MHP SCs and the electrodes, the bulk SCs were meticulously polished with abrasive papers and abrasive pastes before electrode deposition. To assess the impact of SC thickness or device structure on photodetection performance, we conducted an experiment involving the growth of $MAPbBr_3$ and $MAPbCl_3$ monocrystalline films on ITO or SiO_2/Si substrates. The resulting characterization data, as depicted in Figure S2, Supporting Information, aligns with that of the bulk samples. Additionally, SEM images in Figure S2c,f, Supporting Information indicate that both films possess smooth surfaces and uniform shapes. To further characterize $(PEA)_2PbI_4$ monocrystalline films, optical images, SEM images, XRD, PL, and absorption spectra were measured. Figure S3a,b, Supporting Information shows a photograph, a SEM image (inset in Figure S3a, Supporting Information), and an optical image of a typical $(PEA)_2PbI_4$ thin film on a glass substrate. The corresponding PL and absorption spectra are shown in Figure S3c, Supporting Information, with a corresponding bandgap of 2.28 eV. The XRD patterns in Figure S3d, Supporting Information show a series of sharp, intense, and well-defined diffraction peaks repeating periodically, belonging to (00 h) (h = 1, 2, 3...) crystal planes of $(PEA)_2PbI_4$, consistent with reported results.[32]

Nine types of photodetectors were fabricated based on the monocrystalline and centrosymmetric properties of the aforementioned three MHP SCs. The photodetectors were structured as follows: ITO/$MAPbBr_3$/Au Schottky junction, $MAPbBr_3$/Bi Schottky junction, $MAPbCl_3$/Bi Schottky junction, $MAPbBr_3$/Si (n-type) heterojunction, $MAPbCl_3$/Si (n-type) heterojunction, $MAPbBr_3$/PC61BM heterojunction, $MAPbCl_3$/P3HT heterojunction, $(PEA)_2PbI_4$/Bi Schottky junction, and $(PEA)_2PbI_4$/PC61BM heterojunction. Given the demonstrated p-type conducting behavior of $MAPbBr_3$ and $MAPbCl_3$ SCs,[33,34] The Schottky-contacted PDs with a vertical structure were fabricated by growth of $MAPbBr_3$ SCs on ITO glass (4.5 eV), followed by thermal evaporation of 50 nm Au top electrode (a circle with a diameter of one millimeter). For the Schottky-contacted PDs with a lateral structure, the thermally evaporated Bi/Ag electrode with a low work function was deemed appropriate for the formation of Schottky junctions, as Bi avoids the potential issue of corrosion by perovskite.[35] For heterojunctions, the ITO electrode was magnetron sputtered onto MHP SCs directly, to form an ohmic contact. Since the band bending and the depletion region at the junction interface result in the interfacial polarization, polar structures are generated in the depletion region of the centrosymmetric MHPs.

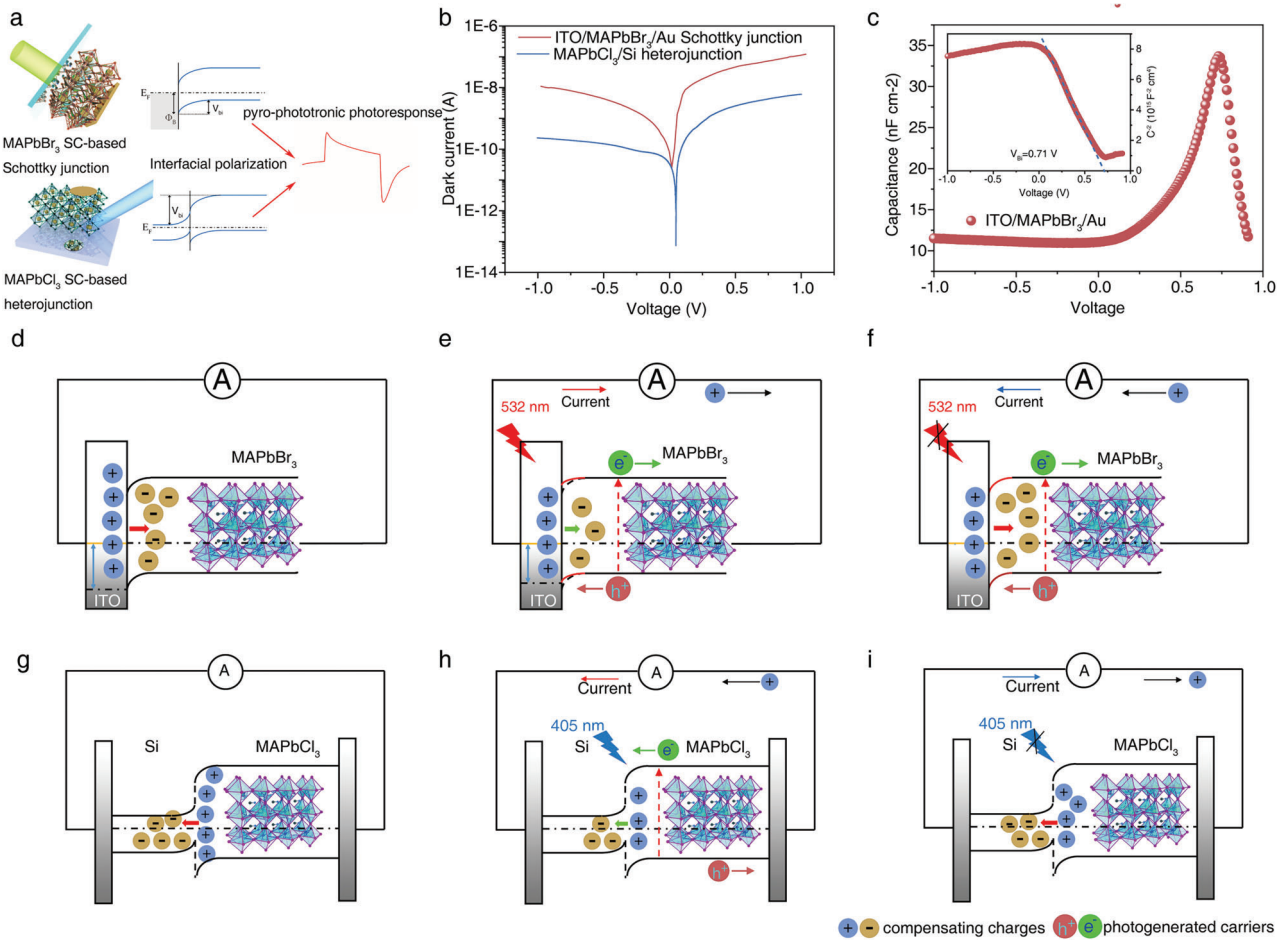

Figure 1. Working principle of interfacial pyroelectric effect enhanced PD based on MHP SC. a) Schematic diagram of the pyroelectric responses of $MAPbBr_3$ SC/ITO Schottky contact and $MAPbCl_3$ SC/Si heterojunction-based PDs with band bending-induced interfacial polarization. b) Current–voltage (I–V) curves of the ITO/$MAPbBr_3$/Au Schottky junction (red one) and $MAPbCl_3$ SC/Si heterojunction (blue one). c) The capacitance–voltage curve of the ITO/$MAPbBr_3$/Au Schottky junction. The inset shows the C^{-2} as a function of bias voltage (Mott–Schottky curves), showing a V_{Bi} of 0.71 V. Schematic energy band diagrams of the d–f) $MAPbBr_3$ SC/ITO Schottky contact and g–i) $MAPbCl_3$ SC/Si heterojunction-based PD at d,g) equilibrium state, at the beginning of the e,h) turning on, and f,i) turning off the laser.

Figure 1a depicts the schematic structures of the ITO/$MAPbBr_3$/Au Schottky junction and $MAPbCl_3$/Si heterojunction-based self-powered PDs. The heterostructure interfaces induce interface polar symmetry through band bending, which generates local polarization and an interfacial pyroelectric effect. First, electrical properties under dark condition have been demonstrated by conducting current–voltage (I–V) and capacitance–voltage measurements (Figure 1b,c and Figure S4, Supporting Information). Both two devices show rectification behavior, with a current ratio of 12 for ITO/$MAPbBr_3$/Au Schottky junction and 35 for $MAPbCl_3$/Si heterojunction. The capacitance of ITO/$MAPbBr_3$/Au Schottky junction at zero bias was about 11 nF cm^{-2}. By performing linear fitting of $C(V)^{-2}$ versus the bias voltage (the Mott–Schottky curve), a V_{bi} (built-in potential) of 0.71 V was obtained (inset of Figure 1c). For $MAPbCl_3$/Si heterojunction, the V_{bi} is 0.796 V (Figure S4, Supporting Information). These electric fields are situated at the interfaces of Schottky junctions or heterojunctions, generating interfacial polarization that serves as the basis for the pyroelectric effect. Consequently, interface polar symmetry-induced pyroelectricity is expected in centrosymmetric perovskite-based optoelectronics. To verify the pyro-phototronic effect-based photoresponse of the PDs, we conducted a systematic measurement of the self-powered photoresponses of nine types of PDs and analyzed the enhancement mechanism of the IPPE. Based on the absorption spectra of $MAPbBr_3$ and $(PEA)_2PbI_4$, the 532 nm laser was chosen as the primary light source, while the primary laser wavelength for $MAPbCl_3$ SC-based PDs was 405 nm. Figure S5, Supporting Information displays the time-dependent photoresponses of four typical PDs, namely $MAPbBr_3$/Bi Schottky junction, $MAPbBr_3$/PC61BM heterojunction, $MAPbCl_3$/Bi Schottky junction, and $MAPbCl_3$/Si heterojunction, under laser illuminations (zero bias). These PDs exhibit distinct and stable four-stage response behaviors, which are repeatable and similar to those reported for pyro-phototronic effect-based PDs. The energy band diagrams depicted in Figure 1d–i serve to elucidate the IPPE phenomenon. To illustrate, we consider the ITO/$MAPbBr_3$/Au Schottky junction as an example. In the state of equilibrium

(Figure 1c), a Schottky junction is established at the interface of p-type $MAPbBr_3$ and ITO. The depletion layer at this interface functions as a slender electric polarization layer, wherein the positive polar charges are situated on the $MAPbBr_3$ side and the negative charges on the metal side, with the polarization direction oriented from ITO to the $MAPbBr_3$. To preserve the electric neutrality of the device, the holes present in the ITO and the electrons in the $MAPbBr_3$ serve as compensating charges. The Schottky junction functions as a barrier to impede the recombination of these compensating charges. During the initial stage, only a dark current can be observed when an external circuit is established. Upon exposure to light, as depicted in Figure 1e, the absorption of light generates electron-hole pairs which are propelled by the built-in electric field, resulting in the production of photocurrent (I_{photo}). Meanwhile, the photo-thermal effect leads to the temperature rise of the Schottky junction. According to the literature, the interface polarizations of the Schottky junctions arise from the work function difference between the metal and semiconductor, namely the built-in electric field.[30] MHPs-based devices with temperature-dependent electrical properties and built-in field, may exhibit a temperature-dependent alteration of interfacial polarization intensity. Consequently, the Schottky junction between $MAPbBr_3$ and ITO experiences a reduction in polarization intensity due to the temperature increase induced by light. This results in a redistribution of charges, leading to the generation of a positive pyroelectric current (I_{pyro}) flowing from the ITO interface to the $MAPbBr_3$ semiconductor through the external circuit (stage II). Upon stabilization of temperature, the I_{pyro} ceases, leaving behind a photocurrent platform (stage III). Finally, when the light is off, the cooling increases interfacial electric polarization (Figure 1e). Additionally, a negative pyroelectric current ($I_{pyro'}$) is generated in the external circuit to facilitate charge redistribution during stage IV. The aforementioned mechanism is also applicable to PDs based on $MAPbCl_3$/Si heterojunctions, where interfacial pyroelectricity is induced by band bending at the p-n junction interface, leading to the generation of pyroelectric currents upon light switching.

Then, the detailed photoresponses performances of the nine PDs toward the laser illumination were systematically measured. First of all, the performances of ITO/$MAPbBr_3$/Au Schottky junction-based PD were studied thoroughly. The optical image of the device is shown in Figure S6, Supporting Information. **Figure 2**a shows the on-off photoresponses of the ITO/$MAPbBr_3$/Au Schottky junction-based PD at 0 bias under 532 nm illumination with power density ranging from 1.27 to 254.7 μW cm^{-2}, all exhibiting obvious transient pyroelectric responses. Figure 2b shows the *I–V* curves of the PD under 532 nm laser illumination with different power intensities. Evident rectification characteristics and photoresponses can be found. The currents extracted from Figure 2a are plotted in Figure 2c as a function of the power density. The peak-to-peak current $I_{pyro+photo}$–$I_{pyro'}$ and photocurrent I_{photo} monotonously increase with the power density increase. Besides, the pyroelectric effect significantly increases the output currents, compared with the photocurrent plateau. To obtain the specific detectivity (*D**), the noise current was first obtained by doing a Fourier transform of the dark current[36] in Figure S7a, Supporting Information, which is about 1.96×10^{-10} A at 0 V bias. As shown in Figure S7b, Supporting Information, the noise current of the PD at a bandwidth of 1 Hz is $\approx 2 \times 10^{-13}$ A $Hz^{-1/2}$. Within the frequency range of 1–500 Hz, the noise current is uncorrelated with frequency. Subsequently, the values for responsivity (*R*) and *D** were computed and graphed as a function of power density, utilizing the equations presented below.

$$R = \frac{\left(I_{photo} - I_d\right)/S}{P} \tag{1}$$

$$D^* = \frac{(BS)^{1/2}}{NEP} = \frac{R_\lambda (BS)^{1/2}}{\overline{i_n^2}^{1/2}} \tag{2}$$

where I_{photo} is the photocurrent, I_d is the dark current, *S* is the active area, *P* is the light power density, *B* is the bandwidth, NEP is the noise equivalent power, $\overline{i_n^2}^{1/2}$ is the root mean square value of the noise current. As shown in Figure 2c (blue one) and Figure S8, Supporting Information, both the *R* and *D** behave with a decreasing tendency upon the increase of the power density. The maximum *R* and *D** are obtained with 190 mA W^{-1} and 8.4×10^{10} Jones at the lowest intensity of 1.27 μW cm^{-2}, respectively. Further, we systematically investigate the thickness-dependent performance of the ITO/$MAPbBr_3$/Au Schottky junction-based PDs. Figure 2d compares dark *I–V* curves of two ITO/$MAPbBr_3$/Au Schottky junction-based PDs based on bulk crystal (0.5 mm) and thin film (25 μm), respectively. The PD based on thin SC behaves with a higher dark current and rectification ratio. Also, the thinner devices have much better performance than the thicker devices, since a larger thickness will lead to the more carrier recombination rate. For thicker SCs, 532 nm photons can only penetrate a fraction of the film thickness, not enough to heat the entire film.

Except for vertical structure, the PDs based on Schottky junction with a lateral structure were also fabricated to the testify the universal working mechanism of IPPE. For ITO/$MAPbBr_3$/Au Schottky-based PDs, the $MAPbBr_3$ SCs directly grew on the ITO, forming a good contact. Therefore, good pyroelectric photoresponses can be obtained. However, for perovskite/Bi-based Schottky junctions, the electrodes were vacuum evaporated onto the SCs surfaces. Since residual liquids may adhere to the crystals during extraction from the stock solution, resulting in additional crystallization and rough surfaces. Besides, interface charge pinning effects can also affect the Schottky junction. First, we investigated the contact type between the metal electrodes and the $MAPbBr_3$ MHPs. To ensure uniform chemical and physical conditions between two electrodes, a set of electrodes (15 nm Bi/100 nm Ag) was deposited onto a (001) crystal surface using a shadow mask. The resulting metal-semiconductor-metal (M-S-M) devices were spaced 20, 50, and 100 μm apart, respectively. Before conducting photoresponse measurements, the dark *I–V* characteristics of the devices were measured to assess the interface contact condition. The observed trend of the dark current exhibits nonlinearity with increasing voltage, suggesting that the interface between perovskite and Bi displays Schottky behavior instead of Ohmic contact, with a turn-on voltage of ≈0.3 V (as depicted in Figure S9a, Supporting Information). Subsequently, the Schottky barrier height (SBH) was ascertained through temperature-dependent *I–V* measurements (as illustrated in Figure S8b, Supporting Information, ranging from

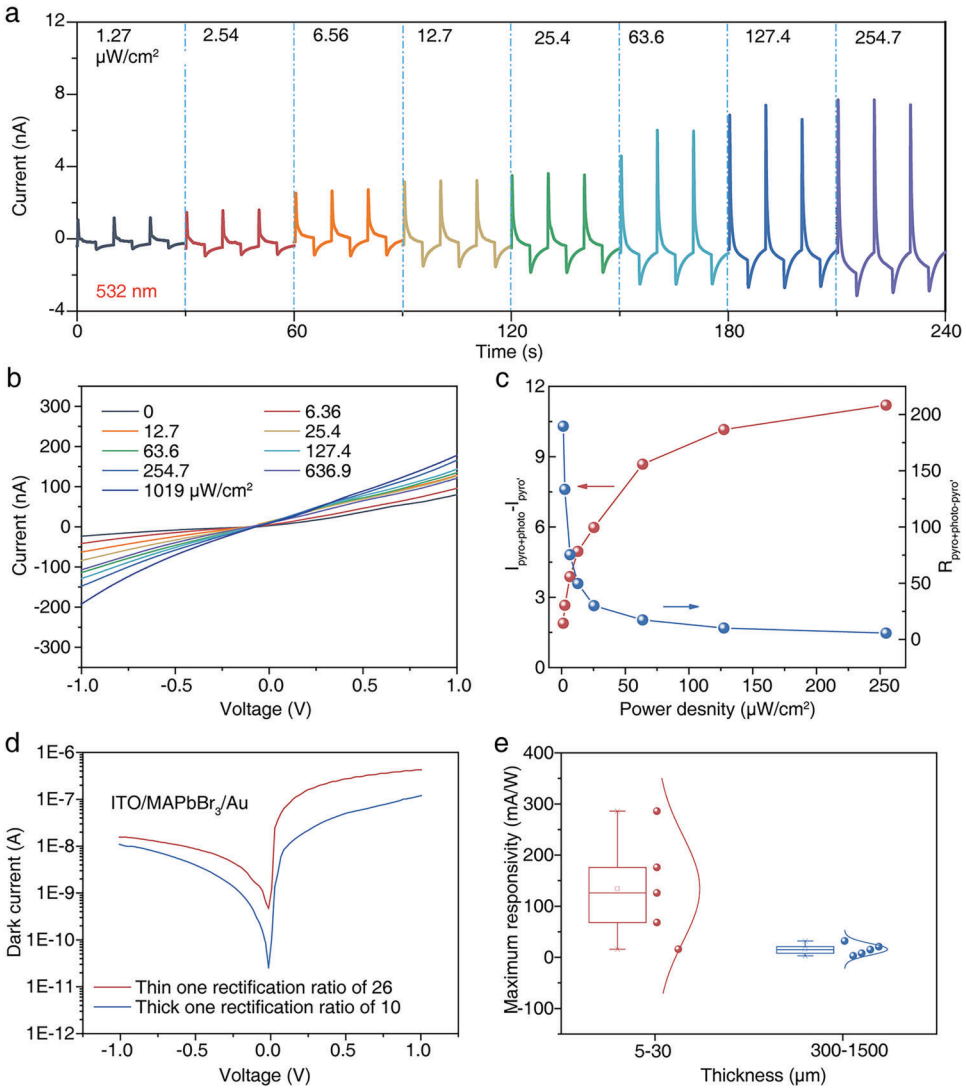

Figure 2. Self-powered performance of the ITO/$MAPbBr_3$/Au Schottky contact-based PD toward 532 nm laser. a) Photoresponses of the PD with different power densities from 1.27 to 254.7 μW cm^{-2}. b) *I–V* curves under 532 nm laser illumination with different power densities from 0 to 1019 μW cm^{-2} under a 1 V bias. c) The output current extracted from a) (red one), the corresponding responsivities (blue one) as a function of the power density. d) Dark *I–V* curves of the ITO/$MAPbBr_3$/Au Schottky junction based on one thick SC (blue one) and thin SC (red one). e) Averaged maximum *R* of ITO/$MAPbBr_3$/Au Schottky contact-based PDs in two thickness ranges.

303 to 373 K). The current density at saturation in the reverse-biased Schottky junction can be mathematically expressed as follows:[34]

$$J = A^* T^2 \exp\left(\frac{-q\Phi_{BE}}{K_B T}\right) \quad (3)$$

where A^* is the equivalent Richardson constant, q is the electron charge, Φ_{BE} is the effective SBH, K_B is the Boltzmann constant, and T is the kelvin temperature. Therefore, the Φ_{BE} can be deduced by plotting ln (J/T^2) as a function of $1/T$. At a bias of 1 V, the Φ_{BE} between $MAPbBr_3$ and Bi was calculated to be 0.39 eV (Figure S9c, Supporting Information). Thus, band bending generates the built-in field at the $MAPbBr_3$/Bi interface.

The photographic representations of PD founded on the $MAPbBr_3$/Bi Schottky junction are depicted in Figure S10a, Supporting Information. The optical images of the effective area of the lateral Schottky junction-based devices, with a spacing of 50 μm, are displayed in the insets of Figure S10a, Supporting Information. Figure S10b, Supporting Information illustrates the *I–V* characteristics of the PD under both dark and light illumination with varying power intensities, all of which exhibit rectifying characteristics. Additionally, the temporal photoresponses of the PD under laser illumination with different power densities (zero bias) demonstrate stable and reproducible photocurrent generation, exhibiting four-stage photoresponse behaviors. The negative pyroelectric current peaks are not prominent, especially under laser illumination with large power densities (Figure S10c, Supporting Information). This phenomenon may

be due to the non-ideal contact induced by image forces and interface pinning effects, leading to the carrier transmission directly across the interface rather than the external circuit. Figure S11, Supporting Information shows the overall self-powered performance of the $MAPbBr_3$/Bi Schottky junction-based PD toward 532 nm laser. The pyroelectric effect significantly increases the output currents, with a maximum enhancement of ≈3.8, compared with the photocurrent plateau (Figure S11c, Supporting Information). The maximum R and D^* are obtained with 138 mA W^{-1} and 2.5×10^{10} Jones at the lowest intensity of 0.014 mW cm^{-2}, respectively. The photoresponses of the self-powered PD toward 360, 405, and 785 nm lasers are shown in Figure S12a–c, Supporting Information, which were also greatly enhanced by the IPPE. Moreover, the PDs also demonstrated pyroelectric response toward near-infrared light (1064 nm), which far exceeds the absorption spectrum of the $MAPbBr_3$ SC. The four-stage response behavior of the I–t curves for three power densities under 1064 nm laser illumination is evident in Figure S12d, Supporting Information. This behavior indicates a significantly expanded range of wavelength response to near-infrared wavelength, in contrast to conventional PDs based on $MAPbBr_3$.[37] As shown in Figure S13, Supporting Information, the PD shows a fast response speed with rise time and fall time of 60 and 410 µs, respectively. Also, the performances of $MAPbCl_3$ bulk SC/Bi Schottky junction-based PD were systematically evaluated in Figure S14–S17, Supporting Information. A peak $R_{pyro+photo}$ of 20 mA W^{-1} was obtained under 405 nm laser illumination. The rise and fall times are 200 and 300 µs, respectively, as illustrated in Figure S17, Supporting Information. Subsequently, we systematically investigate the thickness-dependent performance of the $MAPbX_3$/Bi Schottky junction-based PDs.

We also fabricated lateral Schottky contacts based on $MAPbBr_3$ and $MAPbCl_3$ monocrystalline films. The photoresponse behaviors of film-based PDs were observed to be consistent with those of bulk PDs, as illustrated in Figure S18, Supporting Information. The overall photoresponses of the $MAPbBr_3$ and $MAPbCl_3$ SC film/Bi Schottky junction-based PD are depicted in Figures S19 and S20, Supporting Information, respectively. The observed current peaks in these PDs can be attributed to IPPE, which significantly enhances their overall performance. A total of thirty-eight devices with thicknesses ranging from 3 µm to 2 mm were measured, and the averaged maximum $R_{pyro+photo}$ for each device in the six thickness ranges was calculated and plotted. Generally, the carrier transport distance is determined by the thickness of the MHP, with thinner devices exhibiting superior performance. As depicted in Figure S21a,b, Supporting Information, the performance of the PDs in both $MAPbBr_3$ and $MAPbCl_3$ SCs was found to be unaffected by the thickness of the crystal. This observation further substantiates that the lateral Schottky junction-based PDs rely on the devices' interface rather than the bulk light absorption. Also, $MAPbBr_3$/Bi Schottky junction-based PDs with different electrode gaps (20, 50, and 100 µm) were fabricated to determine and electrode gap-dependent performance of the $MAPbBr_3$/Bi Schottky junction-based PDs (all based on bulk SCs). The dark currents decrease with the increase of the electrode gap (Figure S21c, Supporting Information). However, as shown in Figure S21d, Supporting Information, this factor has no obvious influence on the performances of PDs based on lateral structure, which is quite different from the results in Figure 2e. The reasons behind these phenomena will be discussed later.

The utilization of the IPPE approach facilitates a broad spectrum of self-powered photodetection applications through the mere construction of heterojunctions or Schottky contacts utilizing MHPs possessing centrosymmetry, irrespective of the perovskite type and device structure. Therefore, a series $MAPbBr_3$ SCs-based heterojunctions were fabricated. The photographic representations of PDs founded on the $MAPbBr_3$/Si heterojunction, $MAPbCl_3$/P3HT heterojunction, $MAPbCl_3$/Si heterojunction, and $MAPbBr_3$/PC61BM heterojunction are depicted in **Figure 3**a,d,g,j, respectively. Figure 3b,e,h,k illustrates the I–V characteristics of the four PDs under both dark and light illumination with varying power intensities, all of which exhibit rectifying characteristics. The I–t curves under zero bias of PDs based on the above four heterojunctions are depicted in Figure 3c,f,i,l, all exhibiting four-stage photoresponse behaviors. For heterojunction-based PDs, both the positive and negative pyroelectric current peaks are significant, with $I_{pyro+photo}$ much larger than I_{photo}. To validate the widespread applicability of IPPE in MHP-based photodetectors, we fabricated Schottky contact and heterojunction-based photodetectors using a typical 2D perovskite $(PEA)_2PbI_4$ with a cubic structure. The photodetectors based on $(PEA)_2PbI_4$ exhibited similar photoresponse behaviors, as shown in Figure S22, Supporting Information. These findings suggest that IPPE represents a universal approach for improving self-powered photodetection using MHPs. The IPPE-based photoresponse performances of various heterojunctions, including $MAPbBr_3$/Si, $MAPbCl_3$/Si, $MAPbBr_3$/PC61BM, $MAPbCl_3$/P3HT, $(PEA)_2PbI_4$/Bi Schottky junction, and $(PEA)_2PbI_4$/PC61BM heterojunction, are presented in Figures S23–S32, Supporting Information. The maximum $R_{pyro+photo-pyro'}$ of $MAPbBr_3$/Si heterojunction, $MAPbCl_3$/Si heterojunction, $MAPbBr_3$/PC61BM heterojunction, $MAPbCl_3$/P3HT heterojunction, $(PEA)_2PbI_4$/Bi Schottky junction, and $(PEA)_2PbI_4$/PC61BM heterojunction are obtained as 15, 0.5, 3.4, 0.4, 13 and 85 mA W^{-1}, respectively. Furthermore, the implementation of the IPPE is feasible irrespective of the heterojunction composition. Various perovskite compositions and structures can be chosen for the MHP component, while diverse inorganic or organic semiconductors are available for the non-perovskite components. These findings underscore the importance and versatility of incorporating the IPPE into centrosymmetric-structured MHPs.

To provide further evidence for the pyro-phototronic effect as the cause of the output current peaks observed in the PDs when light is turned on/off, experiments were conducted involving the illumination of $MAPbBr_3$ and $MAPbCl_3$ bulk SCs with various lasers. The resulting real-time temperature changes were recorded using an infrared camera. The data presented in **Figure 4**a,d and Figure S33a,b, Supporting Information demonstrate that laser illumination of the SCs caused an increase in temperature compared to dark conditions. Moreover, as laser power density increased, the magnitude of the light-induced temperature rise also increased significantly. Figure 4b,e illustrate that the highest temperature changes were observed for the wavelengths of 532 nm (for $MAPbBr_3$ SCs) and 405 nm (for $MAPbCl_3$ SCs). Notably, the temperature increase resulting from 532 nm laser illumination with a power of 120 µW onto

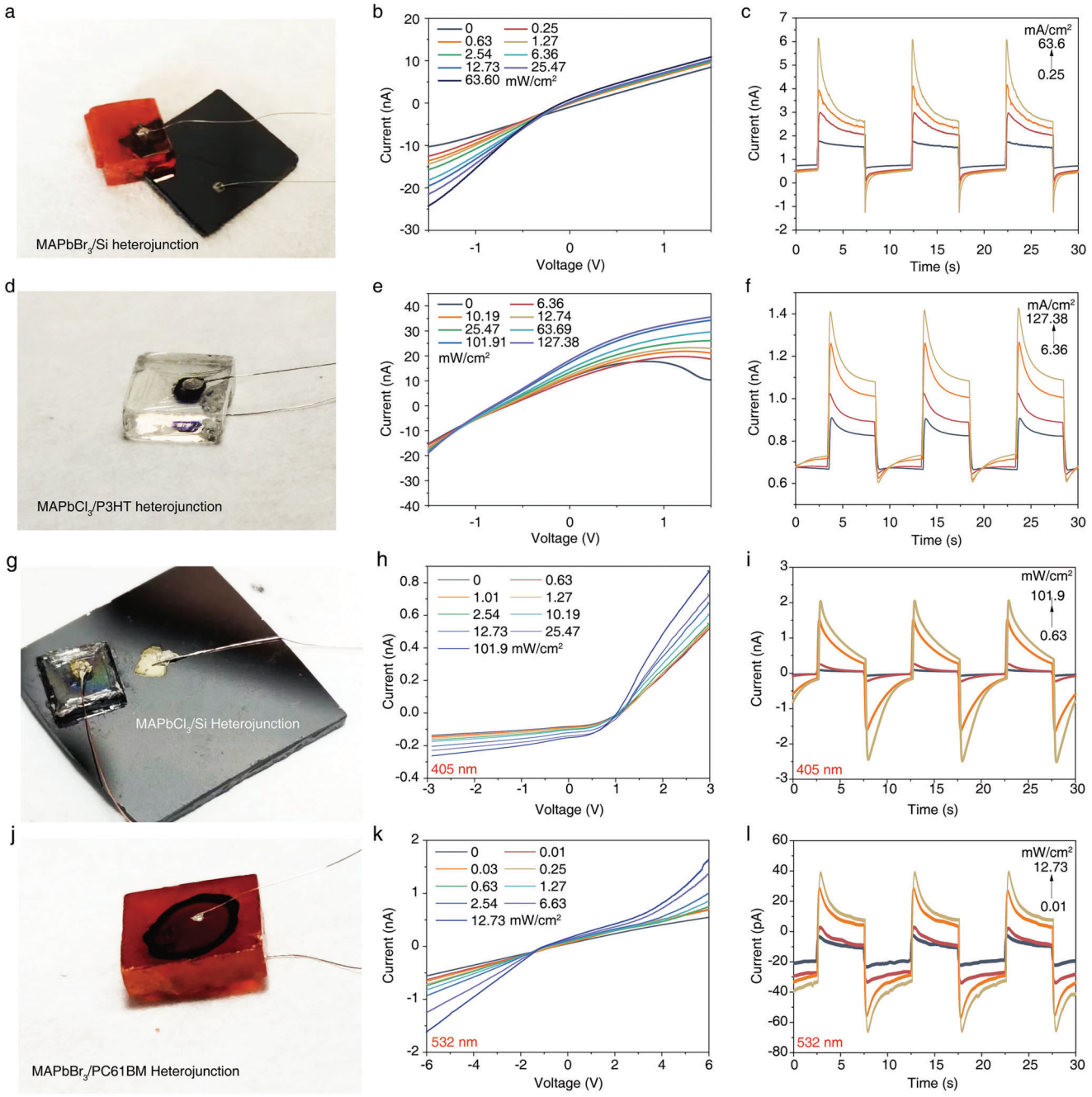

Figure 3. Photographs of a) $MAPbBr_3$/Si heterojunction, d) $MAPbCl_3$/P3HT heterojunction, g) $MAPbCl_3$/Si heterojunction, and j) $MAPbBr_3$/PC61BM heterojunction-based PDs. The corresponding *I–V* curves of the b) $MAPbBr_3$/Si heterojunction, e) $MAPbCl_3$/P3HT heterojunction, h) $MAPbCl_3$/Si heterojunction, and k) $MAPbBr_3$/PC61BM heterojunction-based PDs in the dark and under laser illuminations with different power densities. The *I–t* curves of c) $MAPbBr_3$/Si heterojunction, f) $MAPbCl_3$/P3HT heterojunction, i) $MAPbCl_3$/Si heterojunction, and l) $MAPbBr_3$/PC61BM heterojunction-based PDs. under laser illuminations with different power densities.

$MAPbBr_3$ SC was 4.5 °C, which was considerably higher than those observed for 320, 405, and 785 nm. Similarly, the temperature rise for $MAPbCl_3$ SC illuminated with 405 nm laser (120 μW) was 6 °C, indicating a significant disparity with other wavelengths. Subsequently, we evaluated the spectral photoresponse of the $MAPbBr_3$/Bi Schottky junction and $MAPbCl_3$/Bi Schottky junction-based PDs (Figure 4b,e). All of the photoresponses exhibit the characteristic four-stage photoresponse behaviors, surpassing the bandgap restriction of both $MAPbBr_3$ and $MAPbCl_3$ SCs. The marginal photocurrents observed at 785 and 1064 nm for $MAPbBr_3$ and 532 nm for $MAPbCl_3$ may be attributed to two-photon absorption, which was also found in $FAPbBr_3$[38] and $CsPbBr_3$.[39] Furthermore, it is noteworthy that the maximum response for PDs based on $MAPbBr_3$ is observed at 532 nm, which

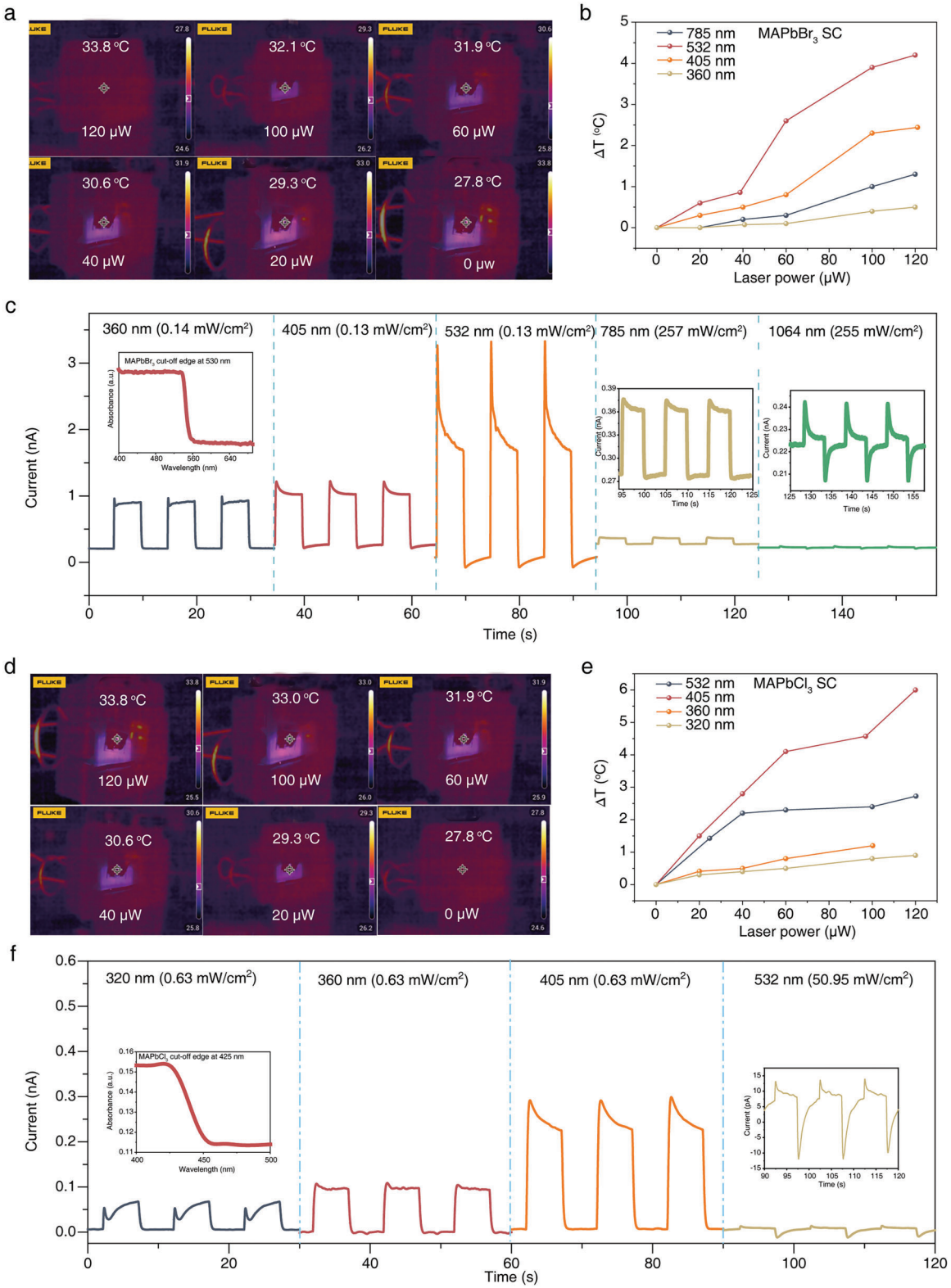

Figure 4. Demonstration of pyroelectric responses. Thermograms of a) the $MAPbBr_3$ SC illuminated with 532 nm laser and d) the $MAPbCl_3$ SC illuminated with 405 nm laser. The temperature of the b) $MAPbBr_3$ SC and e) $MAPbCl_3$ SC when illuminated with different lasers with increased output power. Spectral responses of the c) $MAPbBr_3$ SC/Bi Schottky contact and f) $MAPbCl_3$ SC/Bi Schottky contact-based PDs under laser illumination with different wavelengths at 0 V bias.

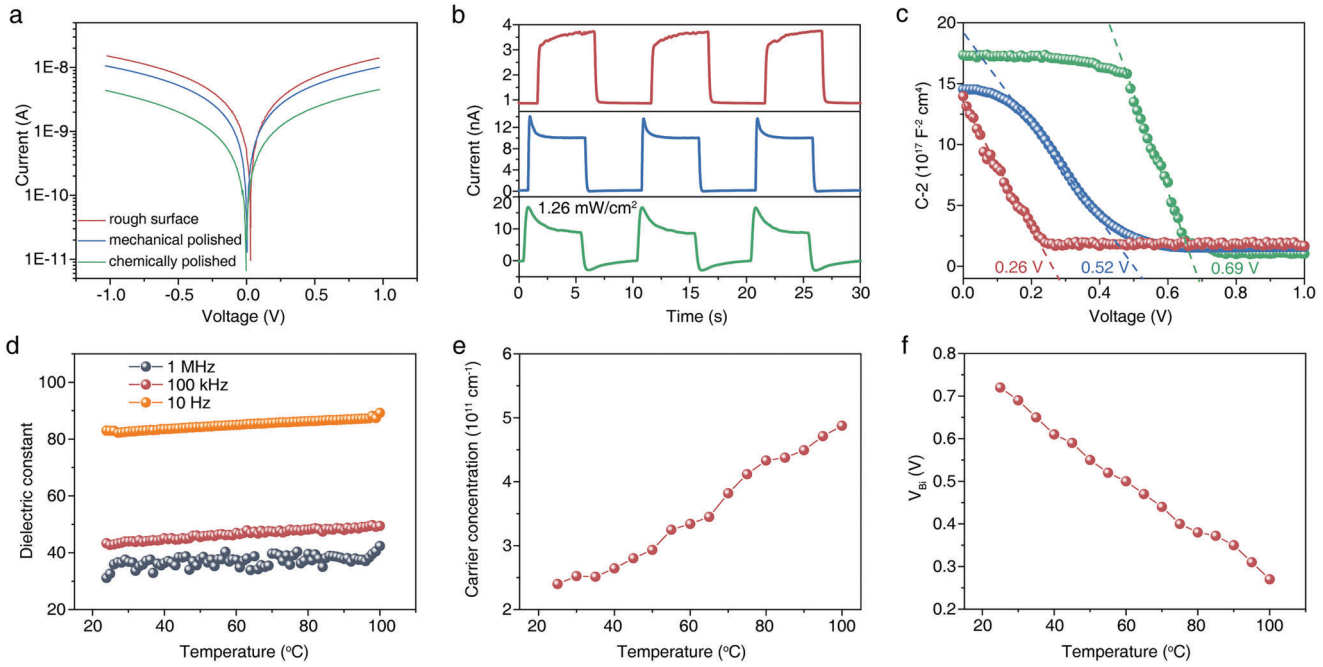

Figure 5. Influence factors IPPE. a) Dark *I–V* curves, b) time-dependent photoresponses, and c) Mott–Schottky curves of the $MAPbBr_3$ SC/Bi Schottky junctions based on SCs with different contact conditions. d) Dielectric constant, e) carrier concentration of the $MAPbBr_3$ SC as a function of temperature. f) V_{Bi} of ITO/$MAPbBr_3$/Au Schottky junction as a function of temperature.

aligns with the absorption spectrum of $MAPbBr_3$. Similar outcomes were obtained for $MAPbCl_3$. Additionally, the pyroelectric current magnitude of PDs based on $MAPbBr_3$ and $MAPbCl_3$ as a function of wavelength is in agreement with the temperature increase depicted in Figure 4b,e, respectively. These findings substantiate that the current peaks are attributed to the interfacial pyroelectric effect.

However, we also found that the temperature rise induced by light illumination is independent of the contact conditions. Therefore, more details of the junction properties that will influence the IPPE are investigated thoroughly. The ITO/$MAPbBr_3$/Au Schottky junction (Figure 2) behaves much better pyroelectric photoresponse performances than the $MAPbBr_3$/Bi Schottky junction (Figure S11, Supporting Information). Also, for $MAPbX_3$/Si heterojunction-based PDs, obvious four-stage photoresponses can be observed in all power density ranges. For perovskite SC/Si or ITO junctions, a layer of halide terminated silane (3-bromopropyltrimethoxysilane or 3-chloropropylrimethoxysilane) was modified before SCs' growth. The terminal halogen atoms can induce the nucleation and growth of SCs, which increases the adhesion toughness at the interface between perovskite and Si or ITO.[40] Therefore, a good interface is formed. However, for perovskite/Bi-based Schottky junctions, the electrodes were vacuum evaporated onto the SCs' surface. The additional crystallization, rough surfaces, and pinning effect will result in a non-ideal contact interface. To prove this deduction, we prepared several SCs with different treatments. Then, a pair of Bi/Ag electrodes was thermal evaporated onto the SC with a gap of 50 µm. The first batch of SCs was only washed with anisole after being taken from the stock solution. The second batch of SCs was mechanically polished with an 80 000 mesh abrasive paste. The third batch of SCs was first mechanically polished with the abrasive paste and then chemically polished with tiny DMF. As shown in Figure S34, Supporting Information, the mechanically polishing led to a much-improved surface roughness than the untreated one. Further chemically polishing could eliminate traces of mechanical polishing. **Figure 5**a compares the dark *I–V* curves of the above three devices. Since the same electrode pair was deposited, the current rectification ratio cannot be determined. With the increase of the surface smoothness, the dark currents decrease obviously. As shown in Figure 5b, when directly used without polishing, the weak photoresponses with no pyroelectric current peaks were found. When only polished with an 80 000 mesh abrasive paste, the enhanced photoresponses with feeblish negative pyroelectric photoresponses can be observed. When SCs were further chemical polished with DMF, the four stage photoresponses were very obvious, just like the ITO/$MAPbBr_3$/Au Schottky junction-based PDs. Mott-Schottky analysis is then used to study the interfaces of three devices with different surface smoothness. With the improvement of the contact between $MAPbBr_3$ and Bi/Ag electrode, V_{bi} obviously increases from 0.26 to 0.69 V. Therefore, the chemically polished one demonstrates significantly improved photoresponses compared with the other two devices. Theoretical research suggests that the depletion width scales with the V_{bi}, which can be caculated according to the following equation:[41]

$$w \approx \left(\varepsilon_r \Phi_{bi}/c\right)^{1/(d-1)} \quad (4)$$

where ε_r is the relative permittivity of the semiconductor, c is the doping level, and $d = 3$ for 3D heterojunctions. Therefore, better contact conditions can lead to higher V_{bi} and wider

depletion width, with enhanced interfacial polarization and enhanced separation efficiency. Also, the SBH also influences the PDs' performances. We further fabricated PDs based on mechanically polished $MAPbBr_3$ SCs using thermal evaporated Au as the electrodes (Figure S35, Supporting Information). Also, the PDs behave the typical four-stage photoresponses, especially at low power densities. However, the performances of Au electrode-based PDs are much weaker than the Bi/Ag electrode-based ones (Figure S36c, Supporting Information), since $MAPbBr_3$/Au contacts have a smaller SBH.[34] For Schottky contact-based PDs, the IPPE originates the band bending and depletion region within the semiconductor/metal interface. The more weakened barriers (bad contact, pinning effect, or small SBH) will lead to the weaker pyroelectric responses, since the redistribution of charge carriers can happen by electron transmission directly cross the interface rather than transport through the external circuit.

Since the $MAPbBr_3$ SCs hardly absorption 1064 nm photon, the 1064 nm laser was used as the heating source to evaluate the pyroelectric coefficient of our PDs. The corresponding pyroelectric coefficient can be expressed by the following equation:[42]

$$p = \frac{J\Delta t}{\Delta T} \tag{5}$$

where J is the measured current density, $\Delta T/\Delta t$ is the temperature change rate. The charge density can be deduced from the I–t photoresponses of the PDs toward 1064 nm laser. Accordingly, the pyroelectric coefficient of the $MAPbBr_3$/Bi Schottky junction (bulk SC, lateral structure, 50 μm, mechanical polished) is 2.6×10^{-4} C m^{-2} K^{-1}. For $MAPbBr_3$/Au Schottky junction (bulk SC, lateral structure, 50 μm gap, mechanical polished), the pyroelectric coefficient is 1.7×10^{-5} C m^{-2} K^{-1}. For $MAPbBr_3$/ITO Schottky junction (vertical structure, thickness of 23 μm), the pyroelectric coefficient is 1.2×10^{-3} C m^{-2} K^{-1}. According to the reference,[30] the interfacial pyroelectric effect originates from the temperature dependence of the dielectric constant, effective dopant density, and built-in potential in junctions. First, we measured the temperature-dependent dielectric constant of the $MAPbBr_3$ SCs (Figure 5d). With the increase of temperature from room temperature to 100 °C, the change rate of dielectric constant is less than 8%, with very small temperature dependence. Also, the temperature-dependent carrier concentrations of the $MAPbBr_3$ SCs were determined by Hall effect measurement. A two-time enhancement from 2.4×10^{11} cm^{-3} to 4.88×10^{11} cm^{-3} was determined (Figure 5e). Furthermore, as shown in Figure 5f, the temperature dependent V_{Bi} of ITO/$MAPbBr_3$/Au Schottky junction was measured by Mott-Schottky measurements. With temperature rising from room temperature, the V_{Bi} declined quickly from 0.736 to 0.27 V. According to the above results, since the dielectric constant has a low temperature dependence, the pyroelectric coefficients of our devices are mainly determined by dependence of the carrier density and built-in potential in junctions. Therefore, the selection of a semiconductor/electrode with suitable energy levels and forming a relative ideal contact is crucial for fabricating high-performance IPPE-based MHP PDs.

Furthermore, we evaluated the influence of the frequency, bias, and operating temperature on the IPPE. Figure S36a, Supporting Information presents the frequency-influenced I–t curves of the $MAPbBr_3$/Bi Schottky contact-based PD under 532 nm laser illumination with a power density of 0.132 mW cm^{-2}. As the frequency increases from 10 to 100 Hz, the photocurrent plateau remains almost unchanged while the $I_{pyro+photo}$ considerably rises, with an enhancement of four times (the blue one in Figure 5b). The response/recovery times extracted from Figure S36a, Supporting Information were plotted as a function of frequency (the red one in Figure S36b, Supporting Information), from which one can see that the response time significantly decreases from 60 to 10 μs, and the recovery time decreases from 410 to 35 μs. For pyroelectric materials based-PDs like ZnO,[42,43] CdS,[8,44] and $MAPbI_3$,[25] the increasing bias severely harms the pyroelectric response. In general, the pyroelectric current vanished within 2–3 V. However, as shown in Figure S36c, Supporting Information, for the $MAPbBr_3$/Bi Schottky contact-based PD, the pyroelectric currents are still evident upon the bias reaching 9 V. Similar results are observed for $MAPbCl_3$/Bi Schottky contact-based PDs and ITO/$MAPbBr_3$/Au Schottky junction, which are shown in Figures S37 and S38, Supporting Information. Therefore, IPPE can also enhance the performance of non-self-powered PDs. However, for $MAPbCl_3$/Si heterojunction, when the reversed bias reaches 3.5 V, the pyroelectric currents vanish (Figure S39c, Supporting Information). In the beginning, we speculated that the joule heat by voltage bias damages the IPPE. However, by performing the temperature-dependent photoresponses measurements, one can see that with the increased operating temperature, although the output currents undergo a continuous declination, the pyroelectric currents never disappear for both $MAPbCl_3$/Si heterojunction-based PD (Figure S36e, Supporting Information) and $MAPbBr_3$/Bi Schottky contact-based PD (Figure S39e, Supporting Information). Like Au/Nb: BSTO junction,[30] the interfacial pyroelectric effect for perovskite/Bi Schottky junction behaves with a weaker temperature dependence than the traditional bulk pyroelectric effect due to the persistence of the depletion region. Then, the voltage-dependent photoresponses of the $MAPbBr_3$/Au Schottky contact-based PD were performed. As shown in Figure S40, Supporting Information, the pyroelectric currents vanished just at a voltage of 0.5 V. Further measurements prove that the voltage limit where pyroelectric currents vanish relies on the SBH. Therefore, we infer that the increasing bias voltage will impair the V_{Bi} and the interfacial polarization. A higher V_{Bi} has advantage in resisting the impair of bias voltage.

3. Conclusions

In summary, a universal IPPE strategy has been introduced for MHP SCs with centrosymmetry to achieve high-performance, self-powered PDs. This strategy facilitates a broad spectrum of applications in self-powered photodetection through the fabrication of heterojunctions or Schottky junctions based on MHPs with centrosymmetry, irrespective of perovskite type and device structure. To verify the universality of the IPPE strategy, nine types of PDs were fabricated with various structures, including ITO/$MAPbBr_3$/Au Schottky junction, $MAPbBr_3$/Bi Schottky junction, $MAPbCl_3$/Bi Schottky junction, $MAPbBr_3$/Si (n-type) heterojunction, $MAPbCl_3$/Si (n-type) heterojunction, $MAPbBr_3$/PC61BM heterojunction,

$MAPbCl_3$/P3HT heterojunction, $(PEA)_2PbI_4$/Bi Schottky junction, and $(PEA)_2PbI_4$/PC61BM heterojunction. All of these PDs exhibited typical pyroelectric photoresponses. By performing the electrical measurements, it is found that the contact conditions are dominant on the IPPE. Forming a heterojunction or Schottky junction with ideal contact will facilitate the efficient separation of charge carriers and the release of compensating charge due to temperature changes. Utilizing the IPPE substantially improves overall performance and a significant expansion of the response spectral range. Furthermore, the IPPE approach can be applied to a broader range of MHP material systems without symmetry limitations. It can be advantageous for developing novel optoelectronic devices.

4. Experimental Section

Materials: *N*, *N*-dimethylformamide (DMF, 99.9%), dimethyl sulfoxide (DMSO, 99.9%), chlorobenzene (CB, 99.5%), cyclohexane (99.5%), and tert-amyl alcohol (99.5%) were purchased from Shanghai Macklin Biochemical Co., Ltd. Lead chloride ($PbCl_2$, 99.99%), methylammonium chloride (MACl, 99.99%), lead bromine ($PbBr_2$, 99.99%), methylammonium bromine (MABr, 99.99%), poly(3-hexylthiophene) (99%), and [6,6]-phenyl C61 butyric acid methyl ester (99%) were purchased from Xian Polymer light Technology Corp. All the chemicals were used as received without further purification.

Growth of the SCs: The $MAPbBr_3$ and $MAPbCl_3$ bulk SCs were prepared using the typical inverse temperature crystallization (ITC) method. For $MAPbBr_3$ SCs, equal molar MABr and $PbBr_2$ (1.5 M) were first dissolved in DMF solvent. For $MAPbCl_3$ SCs, equal molar MACl and $PbCl_2$ (1.8 M) were first dissolved in a mixed solvent (DMSO: DMF = 7:3). To assure complete dissolution, the solution was maintained at 25 °C under active mixing for 24 h, followed by filtration with a 0.22 µm PTFE filter. After transferring 20 mL solution onto the temperature-programmed heating stage, the setup was slowly heated from 25 to 70 °C (for $MAPbBr_3$ SCs) or 25 to 52 °C (for $MAPbCl_3$ SCs) with a slow ramp rate of 1 °C/2 h. The crystallization takes about 24 h after the temperature reaches 70 °C. Crystal with a size larger than 1 cm was selected for device fabrication. For perovskite SCs grown on Si slices or ITO glasses, before the growth of the SCs, the Si (n-type, 1–10 Ω cm) slices and[40] ITO glasses were first modified with halide-terminated self-assembled monolayer according to the previous report.[43,44] For $MAPbCl_3$ and $MAPbBr_3$ SCs grown on Si slices, the modified Si slices were further treated with 3-chloropropyl trimethylsilane and 3-bromopropyl trimethylsilane, respectively. For thin SCs grown on Si/SiO_2 slices, a space-confined ITC method was used, according to the early report.[25]

Fabrication of the PDs: For PDs based on ITO/$MAPbBr_3$/Au Schottky junctions, after the growth of SCs, Au top electrode with a thickness of 50 nm was thermal evaporated onto the SC using a shadow mask (a circle with a diameter of 1 mm). For PDs based on SC/Bi Schottky junctions, the Bi/Ag was selected as the metal electrodes. To form the ideal Schottky junction, the (001) crystal face of the as-prepared bulk SCs was polished with sandpapers (2000 mesh, 5000 mesh, 10 000 mesh, and 80 000 mesh in sequence) before depositing the metal electrodes. No polishing procedures were required for SCs grown on Si/SiO_2 slices. Then, the SCs were thoroughly cleaned and healed according to the literature with some modifications.[45] Cleaning solutions were prepared by mixing cyclohexane and tert-amyl alcohol in a volume ratio of 4:1. Healing solutions were prepared by adding 0.2 mg mL^{-1} MACl (for $MAPbCl_3$) or MABr (for $MAPbBr_3$) into the mixed solution. Finally, 20 nm Bi and 80 nm Ag were successively deposited by a thermal evaporator (0.5 Å s^{-1}) using a shadow mask with a gap of about 20 µm between two electrodes. For PDs based on perovskite/Si heterojunctions, 120 nm ITO and 100 nm Ag were deposited onto SCs and Si, respectively. For PDs based on perovskite/organic semiconductor heterojunctions, P3HT solution in CB (10 mg mL^{-1}) and PC61BM solution in CB (10 mg mL^{-1}) were dipped on the top of the $MAPbCl_3$ bulk SCs or $MAPbBr_3$ bulk SCs, respectively, then annealed at 60 °C for 10 min. After that, Ag and ITO were deposited onto organic layers and SCs, respectively.

Characterization: The XRD patterns were obtained by the Bruker D8 Advance X-ray diffractometer equipped with a Cu tube (λ = 1.5406 Å). UV–vis absorbance spectrum was measured using a Hitachi U4100 UV–vis-NIR spectrophotometer at room temperature, ranging from 250 to 800 nm. Steady-state and time-resolved PL measurements were taken using an FLS920 (Edinburgh Instruments) fluorescence spectrometer with 325 nm excitation wavelength. The surface temperatures of the SCs illuminated with lasers with different wavelengths were recorded by an infrared thermal imager (Fluke TiX1060). The dielectric properties were measured by an LCR meter (TH2828S, Changzhou Tonghui Electronics Co., Ltd.). The capacitance–voltage curves were measured by a semiconductor analyzer (Keysight B1500A). The carrier concentration of the SCs was recorded with a Hall effect test system (Lake Shore 8400).

Photodetection Performance Measurements: The *I*–*V* characteristics and the *I*–*t* curves of the PDs were recorded by coupling a Stanford SRS current preamplifier (SR570) and a Stanford SRS function generator (DS345). The temporal responses of the device were performed on a digital oscilloscope (Tektronix, MDO3104). The laser was periodically switched by transistor-transistor logic potential to generate pulsed laser beams. The 320, 360, 405, 532, 785, and 1064 nm lasers (Changchun New Industries Optoelectronics Technology Co., Ltd.) were used as the light sources and shined onto the top of PDs. The light power intensity was calibrated using a silicon photodiode (PM100D).

Supporting Information

Supporting Information is available from the Wiley Online Library or from the author.

Acknowledgements

L.G., H.W., and Z.X. contributed equally to this work. This work was supported by the National Natural Science Foundation of China (Grant Nos. U20A20166, 62005072, and 62104057), the Natural Science Foundation of Hebei Province (Grant Nos. E2021201016 and B2021201034), the Hebei Education Department (Grant No. BJK2022050), the Advanced Talents Incubation Program of the Hebei University (521000981351 and 521000981248), the Post-graduates Innovation Fund Project of Hebei Province (CXZZSS2022009), and the Science and Technology Plan Project of Hebei Province (Grant Nos. 226Z1002G and 226Z1703G).

Conflict of Interest

The authors declare no conflict of interest.

Data Availability Statement

Research data are not shared.

Keywords

centrosymmetry, interfacial pyro-phototronic effect, metal halide perovskites, self-powered photodetectors, single crystals

Received: June 9, 2023
Revised: August 20, 2023
Published online:

[1] X. Hu, X. Li, G. Li, T. Ji, F. Ai, J. Wu, E. Ha, J. Hu, *Adv. Funct. Mater.* **2021**, *31*, 2011284.
[2] K. Maity, U. Pal, H. K. Mishra, P. Maji, P. Sadhukhan, Z. Mallick, S. Das, B. Mondal, D. Mandal, *Nano Energy* **2022**, *92*, 106743.
[3] Y. Peng, J. Lu, X. Wang, W. Ma, M. Que, Q. Chen, F. Li, X. Liu, W. Gao, C. Pan, *Nano Energy* **2022**, *94*, 106945.
[4] W. Peng, X. Wang, R. Yu, Y. Dai, H. Zou, A. C. Wang, Y. He, Z. L. Wang, *Adv. Mater.* **2017**, *29*, 1606698.
[5] B. Dai, G. M. Biesold, M. Zhang, H. Zou, Y. Ding, Z. L. Wang, Z. Lin, *Chem. Soc. Rev.* **2021**, *50*, 13646.
[6] L. Zhu, Q. Lai, W. Zhai, B. Chen, Z. L. Wang, *Mater. Today* **2020**, *37*, 56.
[7] Q. Zhang, S. Zuo, P. Chen, C. Pan, *InfoMat* **2021**, *3*, 987.
[8] Y. Dai, X. Wang, W. Peng, C. Xu, C. Wu, K. Dong, R. Liu, Z. L. Wang, *Adv. Mater.* **2018**, *30*, 1705893.
[9] Y. Zhang, Y.-C. Wang, L. Wang, L. Zhu, Z. L. Wang, *Adv. Mater.* **2022**, *34*, 2204363.
[10] S. Zhang, S. Ma, B. Cao, Q. Zhuang, Y. Xu, J. Wang, X. Zhang, X. Nan, X. Hao, B. Xu, *Angew. Chem., Int. Ed.* **2023**, *62*, 202217127.
[11] Y. Zhang, J. Chen, L. Zhu, Z. L. Wang, *Nano Lett.* **2021**, *21*, 8808.
[12] J. W. Stewart, J. H. Vella, W. Li, S. Fan, M. H. Mikkelsen, *Nat. Mater.* **2020**, *19*, 158.
[13] J. Jiang, L. Zhang, C. Ming, H. Zhou, P. Bose, Y. Guo, Y. Hu, B. Wang, Z. Chen, R. Jia, S. Pendse, Y. Xiang, Y. Xia, Z. Lu, X. Wen, Y. Cai, C. Sun, G.-C. Wang, T.-M. Lu, D. Gall, Y.-Y. Sun, N. Koratkar, E. Fohtung, Y. Shi, J. Shi, *Nature* **2022**, *607*, 480.
[14] K. Zhao, B. Ouyang, C. R. Bowen, Y. Yang, *Nano Energy* **2020**, *77*, 105152.
[15] M. Kumar, J. Lim, J.-Y. Park, H. Seo, *Small Methods* **2021**, *5*, 2100342.
[16] J. Jeong, M. Kim, J. Seo, H. Lu, P. Ahlawat, A. Mishra, Y. Yang, M. A. Hope, F. T. Eickemeyer, M. Kim, Y. J. Yoon, I. W. Choi, B. P. Darwich, S. J. Choi, Y. Jo, J. H. Lee, B. Walker, S. M. Zakeeruddin, L. Emsley, U. Rothlisberger, A. Hagfeldt, D. S. Kim, M. Grätzel, J. Y. Kim, *Nature* **2021**, *592*, 381.
[17] J. S. Kim, J.-M. Heo, G.-S. Park, S.-J. Woo, C. Cho, H. J. Yun, D.-H. Kim, J. Park, S.-C. Lee, S.-H. Park, E. Yoon, N. C. Greenham, T.-W. Lee, *Nature* **2022**, *611*, 688.
[18] Y. Lei, Y. Chen, R. Zhang, Y. Li, Q. Yan, S. Lee, Y. Yu, H. Tsai, W. Choi, K. Wang, Y. Luo, Y. Gu, X. Zheng, C. Wang, C. Wang, H. Hu, Y. Li, B. Qi, M. Lin, Z. Zhang, S. A. Dayeh, M. Pharr, D. P. Fenning, Y.-H. Lo, J. Luo, K. Yang, J. Yoo, W. Nie, S. Xu, *Nature* **2020**, *583*, 790.
[19] Y. Lei, Y. Li, C. Lu, Q. Yan, Y. Wu, F. Babbe, H. Gong, S. Zhang, J. Zhou, R. Wang, R. Zhang, Y. Chen, H. Tsai, Y. Gu, H. Hu, Y.-H. Lo, W. Nie, T. Lee, J. Luo, K. Yang, K.-I. Jang, S. Xu, *Nature* **2022**, *608*, 317.
[20] C. Qin, A. S. D. Sandanayaka, C. Zhao, T. Matsushima, D. Zhang, T. Fujihara, C. Adachi, *Nature* **2020**, *585*, 53.
[21] J. Zhuang, J. Wang, F. Yan, *Nano-Micro Lett.* **2023**, *15*, 84.
[22] S. Shahrokhi, W. Gao, Y. Wang, P. R. Anandan, M. Z. Rahaman, S. Singh, D. Wang, C. Cazorla, G. Yuan, J.-M. Liu, T. Wu, *Small Methods* **2020**, *4*, 2000149.
[23] W. Zheng, X. Wang, X. Zhang, B. Chen, H. Suo, Z. Xing, Y. Wang, H.-L. Wei, J. Chen, Y. Guo, F. Wang, *Adv. Mater.* **2022**, *35*, 2205410.
[24] L. Guo, X. Liu, L. Gao, X. Wang, L. Zhao, W. Zhang, S. Wang, C. Pan, Z. Yang, *ACS Nano* **2022**, *16*, 1280.
[25] Z. Yang, H. Wang, L. Guo, Q. Zhou, Y. Gu, F. Li, S. Qiao, C. Pan, S. Wang, *Small* **2021**, *17*, 2101572.
[26] Z. Yang, X. Li, L. Gao, W. Zhang, X. Wang, H. Liu, S. Wang, C. Pan, L. Guo, *Nano Energy* **2022**, *102*, 107743.
[27] L. Guo, Y. Qi, Z. Yang, L. Zhao, W. Zhang, X. Wang, H. Liu, G. Yan, S. Wang, C. Pan, *Nano Energy* **2022**, *102*, 107714.
[28] L. Guo, X. Liu, R. Cong, L. Gao, K. Zhang, L. Zhao, X. Wang, R.-N. Wang, C. Pan, Z. Yang, *Nano Lett.* **2022**, *22*, 8241.
[29] Y. Liu, X. Pan, X. Liu, S. Han, J. Wang, L. Lu, H. Xu, Z. Sun, J. Luo, *Small* **2022**, *18*, 2106888.
[30] M.-M. Yang, Z.-D. Luo, Z. Mi, J. Zhao, S. Pei E, M. Alexe, *Nature* **2020**, *584*, 377.
[31] B. Chen, T. Li, Q. Dong, E. Mosconi, J. Song, Z. Chen, Y. Deng, Y. Liu, S. Ducharme, A. Gruverman, F. D. Angelis, J. Huang, *Nat. Mater.* **2018**, *17*, 1020.
[32] Y. Liu, Y. Zhang, Z. Yang, H. Ye, J. Feng, Z. Xu, X. Zhang, R. Munir, J. Liu, P. Zuo, Q. Li, M. Hu, L. Meng, K. Wang, D. M. Smilgies, G. Zhao, H. Xu, Z. Yang, A. Amassian, J. Li, K. Zhao, S. Liu, *Nat. Commun.* **2018**, *9*, 5302.
[33] E. Edri, S. Kirmayer, M. Kulbak, G. Hodes, D. Cahen, *J. Phys. Chem. Lett.* **2014**, *5*, 429.
[34] C.-H. Lin, T.-Y. Li, B. Cheng, C. Liu, C.-W. Yang, J.-J. Ke, T.-C. Wei, L.-J. Li, A. Fratalocchi, J.-H. He, *Nano Energy* **2018**, *53*, 817.
[35] S. Wu, R. Chen, S. Zhang, B. H. Babu, Y. Yue, H. Zhu, Z. Yang, C. Chen, W. Chen, Y. Huang, S. Fang, T. Liu, L. Han, W. Chen, *Nat. Commun.* **2019**, *10*, 1161.
[36] C.-H. Liu, Y.-C. Chang, T. B. Norris, Z. Zhong, *Nat. Nanotechnol.* **2014**, *9*, 273.
[37] Z. Yang, Y. Deng, X. Zhang, S. Wang, H. Chen, S. Yang, J. Khurgin, N. X. Fang, X. Zhang, R. Ma, *Adv. Mater.* **2018**, *30*, 1704333.
[38] F. Zhang, B. Yang, K. Zheng, S. Yang, Y. Li, W. Deng, R. He, *Nano-Micro Lett.* **2018**, *10*, 43.
[39] J. Song, Q. Cui, J. Li, J. Xu, Y. Wang, L. Xu, J. Xue, Y. Dong, T. Tian, H. Sun, H. Zeng, *Adv. Opt. Mater.* **2017**, *5*, 1700157.
[40] Z. Dai, S. K. Yadavalli, M. Chen, A. Abbaspourtamijani, Y. Qi, N. P. Padture, *Science* **2021**, *372*, 618.
[41] Q. Ou, Y. Zhang, Z. Wang, J. A. Yuwono, R. Wang, Z. Dai, W. Li, C. Zheng, Z.-Q. Xu, X. Qi, S. Duhm, N. V. Medhekar, H. Zhang, Q. Bao, *Adv. Mater.* **2018**, *30*, 1705792.
[42] W. Peng, Z. Pan, F. Li, Y. Cai, Y. He, *Nano Energy* **2020**, *78*, 105268.
[43] Y. Zhang, M. Hu, Z. Wang, *Nano Energy* **2020**, *71*, 104630.
[44] Y. Chang, J. Wang, F. Wu, W. Tian, W. Zhai, *Adv. Funct. Mater.* **2020**, *30*, 2001450.
[45] X.-J. She, C. Chen, G. Divitini, B. Zhao, Y. Li, J. Wang, J. F. Orri, L. Cui, W. Xu, J. Peng, S. Wang, A. Sadhanala, H. Sirringhaus, *Nat. Electron.* **2020**, *3*, 694.